



Modulating g-C₃N₄-based van der Waals heterostructures with spatially separated reductive centers for tandem photocatalytic CO₂ methanation

Xi Wu^a, Ruiyu Zhong^a, Xudong Lv^a, Zhuofeng Hu^{a,*}, Dehua Xia^a, Chuanhao Li^a, Bo Song^{b,*}, Shengwei Liu^{a,*}

^a Guangdong Provincial Key Laboratory of Environmental Pollution Control and Remediation Technology, School of Environmental Science and Engineering, Sun Yat-sen University, Guangzhou 510006, PR China

^b National Key Laboratory of Science and Technology on Advanced Composites in Special Environments, Harbin Institute of Technology, Harbin 150001, PR China

ARTICLE INFO

Keywords:

Crystalline g-C₃N₄ nanorods
Van der Waals heterostructures
Axial photoelectrons
Tandem CO₂ photoconversion
Active centers

ABSTRACT

Selective conversion CO₂ to hydrocarbons over g-C₃N₄ photocatalyst remains a great challenge. Herein, efficient photocatalytic CO₂ conversion to CH₄ via a unique tandem pathway is achieved over strongly coupled van der Waals (vdW) heterostructure, composed of K⁺-intercalated crystalline g-C₃N₄ nanorods (CCNR) and N-doped porous carbon (NPC). A superior CH₄ selectivity of 90.2% with an outstanding evolution rate of 11.79 μmol g⁻¹ h⁻¹ is demonstrated over optimized CCNR-NPC vdW heterostructure decorated with Pt species, without any sacrificial agents. The radial (intralayer) photoelectrons and axial (interlayer) photoelectrons transfer towards the exposed terminal NH_x-sites at CCNR edge and the NPC-immobilized Pt-sites, respectively, giving rise to two separated spatially but cooperative reductive centers. At terminal NH_x-sites, CO₂ is activated to *CO intermediates, which are hydrogenated into CH₄ at NPC-immobilized Pt-sites. This work will offer a new perspective for selective tandem photocatalytic CO₂ conversion by designing hybrid photocatalysts with spatially separated but cooperative active centers.

1. Introduction

The artificial photosynthesis, involving semiconductor-mediated photocatalytic CO₂ reduction reaction (CO₂RR), is one of the most promising ways contributing to achieving carbon neutral and producing renewable solar fuels (e.g. CO, CH₄, C₂H₄, etc.) [1–4]. g-C₃N₄ is a mostly investigated polymeric semiconductor photocatalyst, with suitable band structures satisfying the thermodynamic requirements of CO₂RR [5]. Unfortunately, the inferior efficiency and selectivity of g-C₃N₄ severely restrict its practical applications [6,7].

Structurally, g-C₃N₄ is characteristic of a graphite-like layered structure. Typically, for the bulk g-C₃N₄ (BCN), prepared by conventional thermal polymerization, both intralayer and interlayer interactions are weak intermolecular forces. Specifically, in-plane polymeric melon chains with terminal amino groups are linked by hydrogen bonding (Fig. 1a), while the π-conjugated CN layers are interconnected by weak van der Waals (vdW) interaction (Fig. 1b) [8,9]. As a result, the photoelectron transport across the intralayer melon chains and the CN layers is largely restrained (Fig. 1a, b), leading to high

charge transport barrier, sluggish charge dynamics, and thus inferior photocatalytic efficiency [8]. In this regard, strengthening the intralayer and/or interlayer interactions between adjacent building units would significantly promote charge flow within g-C₃N₄ framework. This assumption is readily demonstrated by improving intralayer charge transport via enhancing the degree of polymerization (or crystallinity), that is essentially breaking the in-plane weak hydrogen bonding (Fig. 1c), exemplarily in the case of crystalline g-C₃N₄ nanorods (CCNR) formed through widely employed molten salt method [6,10–12]. Nonetheless, it is still a big challenge to strengthen interlayer interactions and to promote interlayer charge transport, while the interlayer charge transport barrier is relatively even much higher. [8] Based on DFT calculations, intercalating interlayer alkali metals (e.g. K⁺) may strengthen the internal vdW interaction between homogenous CN layers, and establish interlayer electronic shuttling channel [13], reducing the barrier for axial photoelectron migration (Fig. 1d). Besides those efforts, constructing interfacial vdW heterostructures by assembling heterogeneous layers of matching 2D nanomaterials (e.g. carbon layers) is also promising in accelerating interlayer charge flows, as

* Corresponding authors.

E-mail addresses: huzhf8@mail.sysu.edu.cn (Z. Hu), songbo@hit.edu.cn (B. Song), liushw6@mail.sysu.edu.cn (S. Liu).

<https://doi.org/10.1016/j.apcatb.2023.122666>

Received 6 December 2022; Received in revised form 11 March 2023; Accepted 18 March 2023

Available online 21 March 2023

0926-3373/© 2023 Elsevier B.V. All rights reserved.

illustrated by CN/C vdW heterostructures with even lower interfacial charge transport barrier (Fig. 1 h) [14–16]. Thereinto, N-doped porous carbon (NPC, Scheme S1) is an ideal candidate for building interfacial CN/C vdW heterostructures, owing to interfacial compatibility for growing CCNR photocenters and decorating Pt active sites [17,18]. Moreover, NPC may work as excellent CO₂RR active centers by gathering both photoelectrons and CO₂ reactant molecules. Based on the above discussion, the interlayer K⁺-intercalation and interfacial NPC hybridization can be combined to internally and externally strengthen the axial vdW interactions of CCNR and significantly accelerate the cross-layer photoelectron transport (Fig. 1e).

The charge utilization at active sites determines CO₂RR efficiency and selectivity. The reduction active sites not only collect the photoelectrons, but also adsorb and activate CO₂ and its reduction derivatives (e.g. CO) [19,20]. The linear scaling relationship restricts the differential tuning on adsorption behaviors of two different kinds of surface species at one single kind of active site [21]. Complex reaction steps and multiple reaction intermediates are involved during CO₂RR, necessitating distinct active sites regulating the specific molecule-catalyst

interaction, and the surface adsorption/desorption processes [22]. The terminal NH_x-moieties (including -NH₂ and/or -NH) on the surface (e.g. BCN) and/or at the edge (e.g. CCNR) of π -conjugated CN layers are dominant active sites for pristine g-C₃N₄, causing infertile CO₂ adsorption and competitive desorption versus hydrogenation of *CO intermediate, and thus the CO₂RR product is mainly limited to CO [23,24]. To produce hydrocarbons (e.g. CH₄), stabilizing *CO intermediate at additional active sites (or integrated multifunctional active sites [25]) for further hydrogenation is necessary. To this end, designing tandem catalytic centers [26,27], separated spatially but coupled sequentially, has emerged as one of the most promising strategies. In this study, after manipulating radial and axial charge transports in CCNR-NPC vdW heterostructures, while the radial photoelectrons are enriched on the CCNR edges, the axial photoelectrons will be collected on the NPC-immobilized Pt species, giving rise to two different kinds of spatially separated reduction active centers. The NH_x-sites at CCNR edges adsorb and transform CO₂ to *CO, which are subsequently captured and hydrogenated into CH₄ over nearby NPC immobilized Pt active sites (Fig. 1e), together improving the CO₂RR selectivity to CH₄,

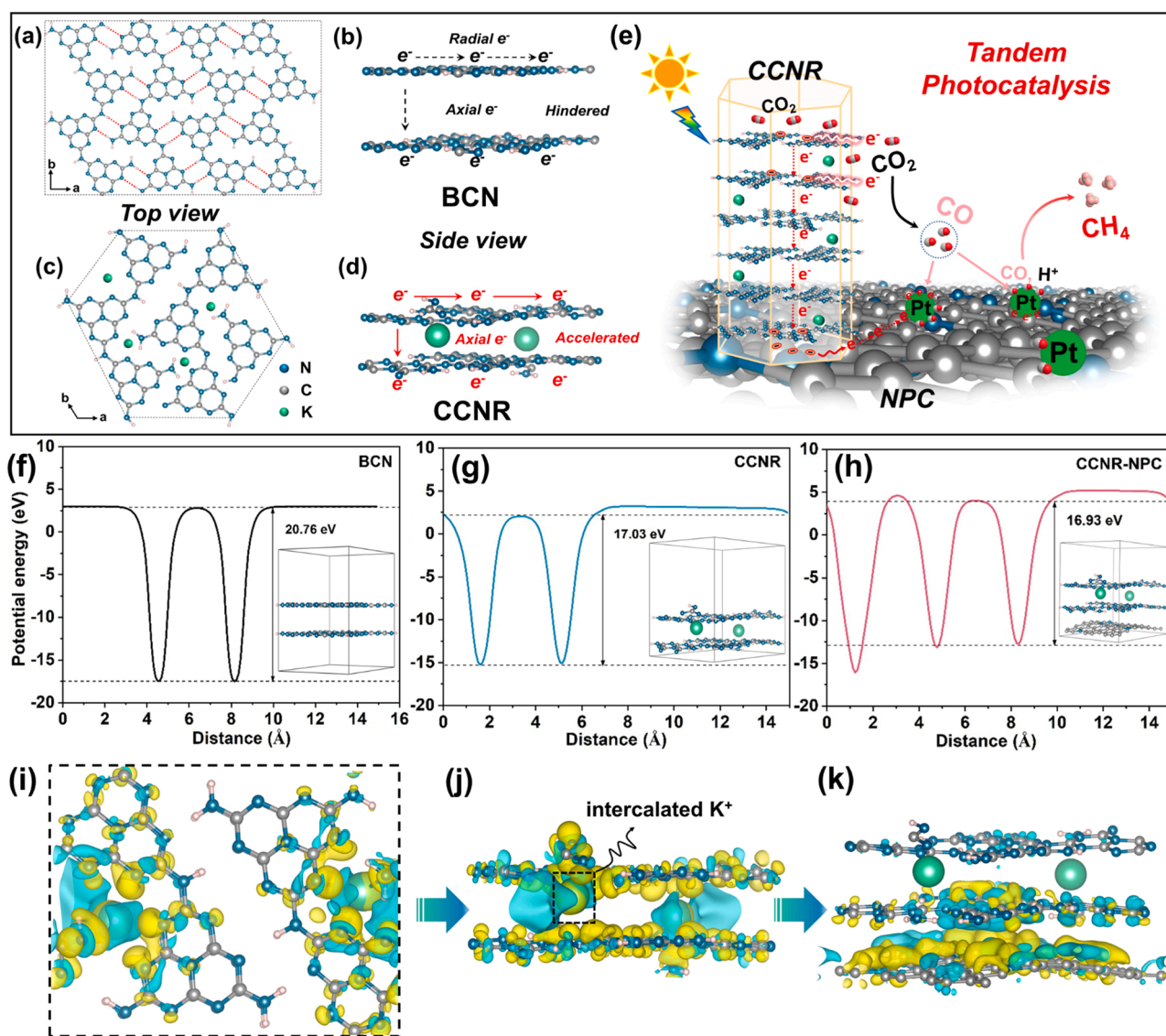


Fig. 1. (a–d) Top (left) and side (right) view of the atomic structure of pristine BCN and CCNR. (e) The hypothetical tandem photocatalytic CO₂RR mechanism over CCNR-NPC/Pt. The calculated interlayer electrostatic potentials and optimized local structures (inset) for (f) BCN, (g) CCNR and (h) CCNR-NPC samples. The calculated differential charge density distribution for CCNR, top (i) and side (j) views, and for CCNR-NPC, side view (k); Thereinto, charge accumulation is shown in yellow and depletion in blue. Gray, blue, green, red and pink spheres represent C, N, K, O and H atoms, respectively.

up to 90.2%. This work will provide new perspectives for highly selective photocatalytic CO₂ methanation through a tandem route over vdW heterostructures by manipulating intralayer and interlayer photoelectrons transfer and utilization simultaneously.

2. Experimental section

2.1. CCNR-NPC photocatalysts preparation

The CCNR-NPC photocatalysts were achieved via an ionothermal synthesis approach. Typically, 7 mg of NPC and 3 g melamine were uniformly dispersed in 60 mL deionized water to form homogeneous-like solution by vigorous agitation, whereafter ultrasonicated for 30 min. The mixture was subsequently dehydrated at 80 °C for 8 h. The dried samples were crushed and placed on the corundum porcelain boat of muffle furnace for 4 h of heating at 500 °C with 5 °C/min rate. After naturally cooling, the pre-heated sample was ground with a mixture of LiCl/KCl (molar ratio 59:41) in a mortar, followed by heating at 550 °C for 4 h with 2.5 °C/min rate under a N₂ flow in the tubular furnace. After cooling to room temperature naturally, the resulting sample was washed with boiling deionized water to remove residual salt and air-dried at 60 °C for 8 h. The obtained sample was denoted as CCNR-NPC. Reference samples of CCNR-NPC-X (X = 1–6) were prepared using the similar procedure, except that the added NPC amount was 1 mg, 3 mg, 5 mg, 6 mg, 8 mg, and 9 mg. Additionally, BCN-NPC was also prepared following similar procedures, except that BCN was used instead of CCNR. For comparison, CCNR was synthesized by the same procedure without adding NPC, and pristine BCN was directly heated melamine at 550 °C for 4 h with 5 °C/min rate.

Experimental details of the sample preparation, schematic diagram of the formation process of typical samples, characterization, photoelectrochemistry measurements, DFT calculations and photocatalytic CO₂RR measurements were provided in sections S1&S2 of [Supporting Information](#).

3. Results and discussion

3.1. Crystal phase and microstructures

Based on the calculation of the interlayer electrostatic potentials of BCN, CCNR and CCNR-NPC (Fig. 1f–h), intercalating K⁺ and hybridizing NPC can reduce the interlayer distance (Table S1) and reduce the interlayer electrostatic barrier from the original 20.57 eV (BCN) to 17.06 eV (CCNR) and 16.93 eV (CCNR-NPC). Strengthening interlayer interaction is essential, while additional Pt decoration has little effect on decreasing the interlayer electrostatic barrier (Fig. S1). Moreover, the charge redistribution, reflected by calculating differential charge density (Fig. 1i–k), reveals that intercalated K⁺ have strong interaction with the cave N atoms from adjacent upper and lower two CN layers (Fig. 1j and k), building expedite interlayer electronic transfer bridge. Meanwhile, the charges orient toward NPC at the interface of CCNR-NPC vdW heterostructures (Fig. 1h). Enhancing internal/interfacial interactions and building cross-layer charge transfer channels within CCNR-NPC synergistically facilitates axial electron diffusion. Taking account of the promoted radial photoelectrons transfer along π -conjugated CN layers because of higher degree of polymerization of CCNR, the simultaneously facilitated radial/axial charge flow across CN layers and CN/C interface, together not only promote the overall charge dynamics, but also give rise to two spatially separated reduction active sites with enriched photoelectrons, promising tandem photocatalytic CO₂RR to CH₄ (Fig. 1e).

The CCNR-NPC vdW heterostructures were constructed by a typical LiCl/KCl-mediated molten salt method, using preformed NPC to support the vertical growth of CCNR (Scheme S2). The morphologies and microstructures are observed by combining scanning electron microscopy (SEM) and transmission electron microscopy (TEM). NPC exhibits a

flaky architecture composed of hollow and cubic lamellas (Fig. 2a, inset), and the average size of individual granules is \approx 20 nm (Fig. 2a). As usual, bare BCN displays common stack-like bulk morphology that consists of the accumulated and compact carbon nitride nanoplates (Fig. S2a). In contrast, NPC-supported CCNR present uniform nanorods with the diameter of 20–30 nm and length of 400–500 nm (Fig. 2b and S2b), which is consistent with the corresponding side-view TEM result (Fig. 2c). Note that, most nanorods were grown along the poriferous channel of NPC (Fig. 2d and S2c), favoring for collecting the axial photoelectrons from the CCNR. The high-resolution TEM image of an individual nanorod (Fig. 2e) indicated the lattice fringes with a (100) spacing of 1.116 nm (inset of Fig. 2e), suggesting that the growth direction of CCNR is along the c-axis [28]. Prominently, a portion of the top-view CCNR ends with a hexagonal cross-section (inset of Fig. 2b), suggesting the six-fold hexagonal symmetry of intralayer arrangements of building units (Fig. 1c).

The powder X-ray diffraction (XRD) pattern (Fig. 2f) and FTIR spectra (Fig. S3a) of CCNR-NPC are almost the same as that of CCNR, but are very different from that of BCN. Two typical XRD peaks at 13.1° and 27.5° were observed for conventional BCN (Fig. 2f), corresponding to (100) and (002) crystal planes, respectively [29,30]. Because of the increased degree of polymerization and extended π -conjugated units of CCNR versus BCN, the (100) diffraction peak prominently shifts from 13.1° to 8.0°. Meanwhile, owing to reduced interlayer spacing and enhanced interlayer interaction within CCNR versus BCN, the (002) diffraction peaks shift from 27.5° to 28.0°. On the basis of Bragg equation $d_{hkl} = \lambda / (2\sin\theta)$ in JADE, the lattice distance of the in-planar periodic caves enlarges from 0.679 nm to 1.107 nm and the interlayer distance is reduced from 0.334 nm to 0.328 nm. Relative to BCN, both the intralayer interactions and interlayer interactions are reinforced within CCNR, which is reserved in CCNR-NPC vdW heterostructures. The FTIR spectra (Fig. S3a) show a characteristic vibration peak of tri-s-triazine cycles at 808 cm⁻¹ for BCN. Owing to interlayer π - π interaction between triazine units, a notable shift has occurred in CCNR [15]. Moreover, as a result of breaking hydrogen bonds by molten-salt treatments, more terminal NH_x-moieties are exposed at the edges of CCNR, and the corresponding FTIR signal intensity around 3200 cm⁻¹ for CCNR is higher than that of BCN [31,32]. Furthermore, relative to BCN, it is noted that the peak at 1234 cm⁻¹ red shifts to 1150 cm⁻¹ and the peak at 705 cm⁻¹ blue shifts to 726 cm⁻¹ for the CCNR sample in Raman spectra. These shifts are influenced by the interlayer-stacking and size of the in-planar heptazine units (Fig. S3b). It is further evidence to support that the crystal orientation of carbon nitride has changed due to the internal van der Waals heterostructures, which is consistent with the observation from XRD results. As to CCNR-NPC hybrid, two typical Raman peaks of NPC can be found at 1362 and 1589 cm⁻¹, corresponding to the verified D and G bands of the carbon matrix, respectively. Notably, the overall weakened Raman-active of CCNR-NPC at 1150 and 726 cm⁻¹ was confirmed due to the background shielding effect of the carbon material (Fig. S3b).

The surface compositions and elemental states were identified by X-ray photoelectron spectroscopy (XPS). BCN and CCNR shared similar C 1s spectra (Fig. 3a), in which two peaks located at 284.8 and 288.2 eV were assigned to the sp² bonded C in the standard reference carbon and the N = C–N coordination, respectively [29,30]. By contrast, in CCNR-NPC, because of additional contribution from NPC moiety, the sp² C–C signal is significantly increased, and another peak at 286.5 eV (Fig. S4a) emerged, originating from C–O groups in NPC [10]. Accordingly, two Raman peaks at 1362 and 1589 cm⁻¹ associated with typical D and G bands of carbon matrix, respectively, can be recorded for CCNR-NPC (Fig. S3b). The N 1s spectra (Fig. 3b) can be fitted into three components of C=N–C (398.6 eV), N–(C)₃ (399.5 eV) and C–N–H (400.7 eV) [33]. Notably, in comparison to BCN, CCNR possesses more marginal NH_x-moieties, resulting in an increase in the signal intensity for C–N–H species. These NH_x-moieties are reserved in CCNR-NPC, which would serve as adsorption sites for CO₂ through hydrogen bond

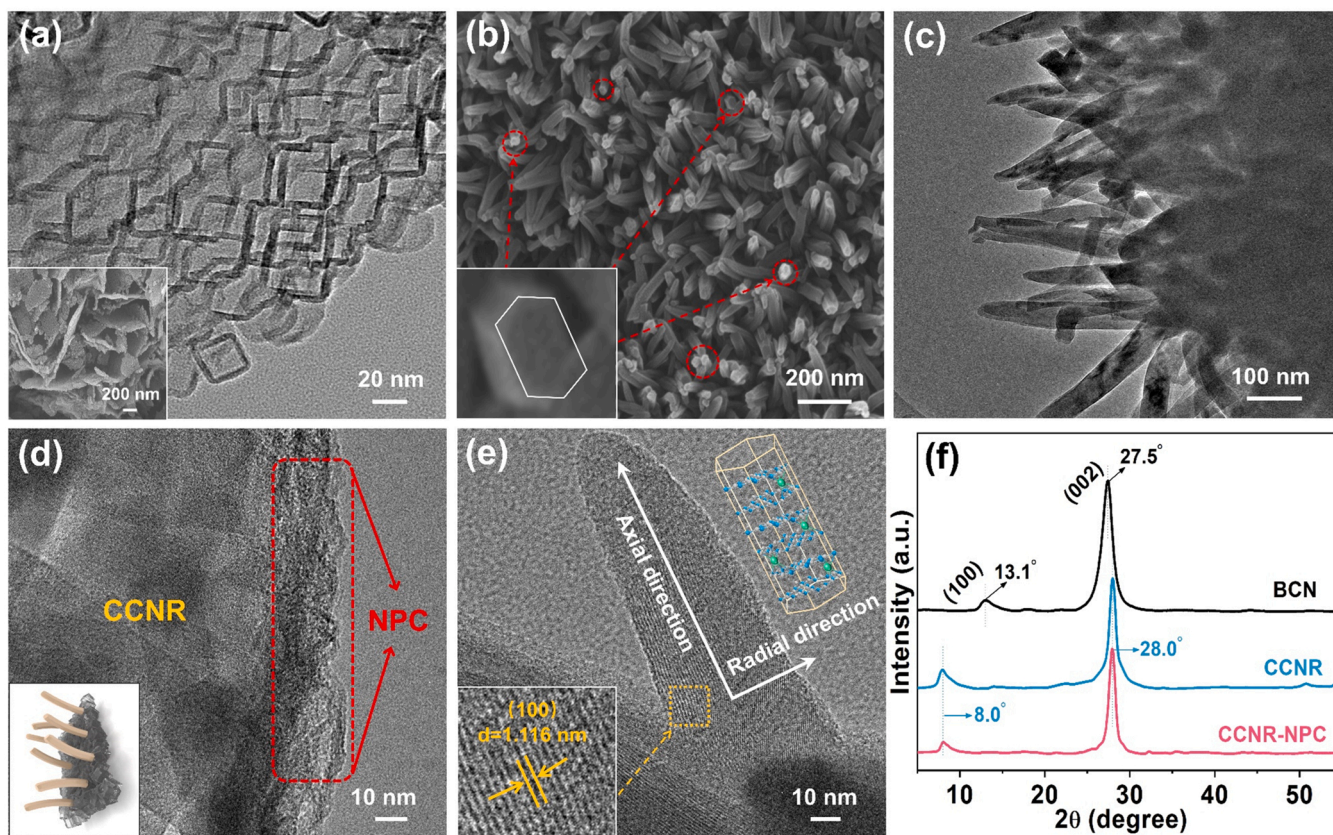


Fig. 2. (a) TEM images of NPC, inset: SEM image; (b) SEM morphological analysis of CCNR, inset: top-view SEM image; TEM image of (c) CCNR and (d) CCNR-NPC, inset: descriptive graph of CCNR-NPC; (e) HRTEM images of CCNR, inset: atomic structure of CCNR; (f) XRD patterns of BCN, CCNR, and CCNR-NPC.

interactions [34]. Note that, the XPS signal of the pyridinic N (398.6 eV) and graphitic N (401.1 eV) observed in NPC (Fig. S4a) are not visible in CCNR-NPC sample [35,36]. Significantly, certain positive shifts in N = C-N₂ and C-N = C groups are observed in CCNR-NPC relative to that in CCNR, confirming that the strong interfacial electronic interaction is formed between CCNR and NPC, and NPC component acts as electron acceptor.

The interlayer K⁺ intercalation in CCNR is demonstrated by the corresponding K 2p spectrum (Fig. 3c), with two notable peaks at 293.0 eV (K 2p_{3/2}) and 295.7 eV (K 2p_{1/2}), which are also maintained in CCNR-NPC. The intercalated K⁺ tend to coordinate with electron-rich N atoms within the cavity surrounded by adjacent tri-s-triazine units (Fig. 1c, d) [37]. Prominently, NPC with abundant N-moieties (Fig. S4a) and highly porous frameworks (Fig. S5a) favor anchoring Pt species [18]. The highly-dispersed Pt species decorated on CCNR-NPC, unfortunately, cannot be detected by XRD, SEM and TEM, are identified by high-resolution XPS. For Pt/BCN and Pt/CCNR, the high-resolution Pt 4f XPS spectra (Fig. 3d) can be deconvoluted into two peaks at about 72.3 eV and 75.5 eV, corresponding to Pt 4f_{7/2} and Pt 4f_{5/2} of metallic Pt, respectively, which confirmed the successful loading with Pt nanoparticles [38]. In sharp contrast, the Pt 4f peaks for CCNR-NPC/Pt, reserving only a minor portion of metallic Pt, are mainly assigned to the Pt-N bonding [18,39]. The unique chemical states of Pt species in CCNR-NPC/Pt are further confirmed by CO adsorption using in situ DRIFTS spectra (Fig. 3e and f). Two bands centered at 2151 and 2185 cm⁻¹ were observed by adsorbing CO until saturation. After that, upon continuous He purging, while the 2185 cm⁻¹ peak associated with gaseous CO or physically adsorbed CO will be completely removed, the CO adsorption peak at 2151 cm⁻¹ was still strong, which was associated with characteristic Pt^{δ+}-CO species [40]. The systematical characterizations clearly demonstrated that well-defined CCNR with abundant intercalated K⁺ are mostly standing on NPC with strong interfacial

electronic interaction, and the decorated Pt species are highly dispersed on NPC with strong Pt-N bonding, which together would accelerate the directional charge flows.

3.2. Charge dynamics characteristics

The charge generation capacity is determined by the optical absorption, reflected by UV/Vis diffuse reflectance spectroscopy (DRS, Fig. 4a). The absorption edge for BCN is 464 nm, which is shifted to 476 nm for CCNR, along with a minor tailing. Significantly, because of the increased degree of polymerization and extended π -conjugated units of CCNR versus BCN, CCNR exhibited significantly enhanced UV light absorption in $\pi - \pi^*$ transition regions [6]. After forming CCNR/NPC interfacial vdW heterostructures and decorating Pt species, π -electron delocalization would be promoted, while the UV light absorption is slightly shielded, the tailing in the visible light and NIR region is somewhat elevated [41]. Overall, compared to BCN, both the light absorption range and intensity have been significantly enhanced, which provide abundant photons to excite CCNR-based photocatalysts, yielding more photoelectrons.

The charge separation and transport dynamics were investigated by steady-state photoluminescence (PL) and time-resolved PL spectra with a 360 nm excitation wavelength. The steady-state PL emission peak centered around 470 nm, being close to the value of the absorption edge (Fig. 4a), was related to the band-to-band recombination of photoelectrons and holes. Clearly, steady-state PL signals were substantially quenched from BCN to CCNR-NPC/Pt (Fig. 4b), indicating that the accelerated radial/axial π -electron delocalization cooperatively inhibited radiative recombinations. The time-resolved PL decay curves (Fig. 4c), recorded at an emission wavelength of 470 nm, can be well-fitted with the triexponential model (Equation S6). Short lifetime (τ_1) is related to radiative exciton recombination, while the long lifetimes, τ_2

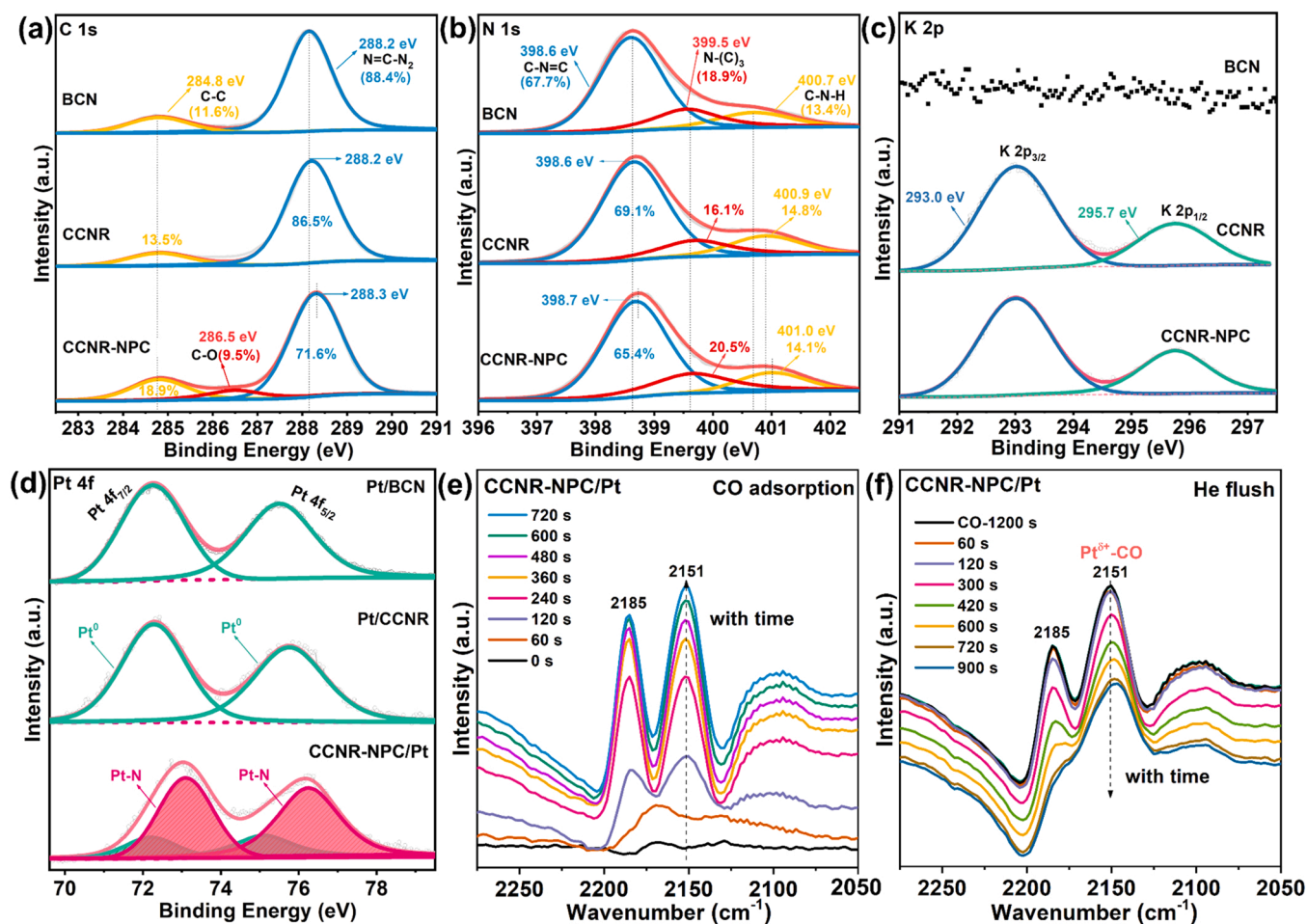


Fig. 3. XPS analyses of (a) C 1s, (b) N 1s, (c) K 2p and (d) Pt 4 f for typical samples; CO-DRIFTS spectra: (e) CO adsorption and (f) CO desorption over CCNR-NPC/Pt.

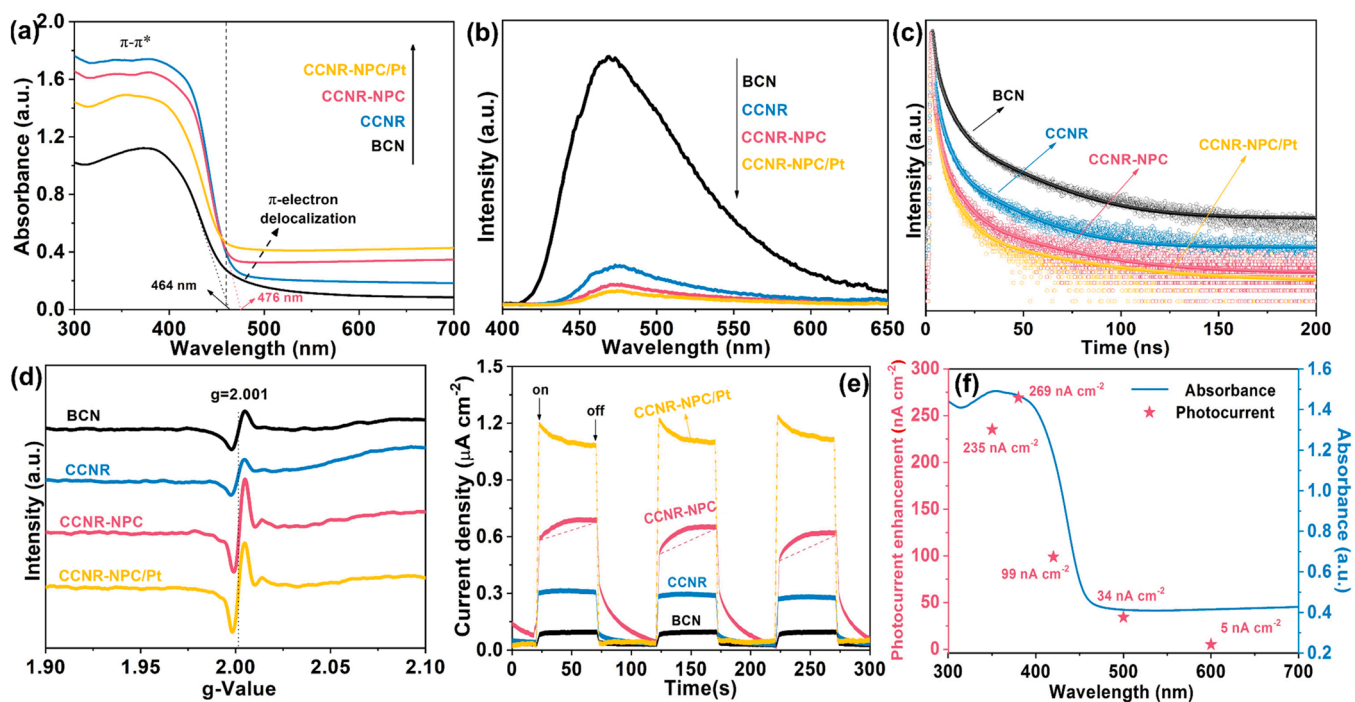


Fig. 4. Charge dynamics. (a) UV/Vis DRS spectra; (b) steady-state PL spectra; (c) time-resolved PL spectra; (d) EPR spectra and (e) the transient photocurrent responses of typical samples; (f) wavelength-dependent photocurrent enhancement for CCNR-NPC/Pt.

and τ_3 , are assigned to nonradiative charge recombination and energy transfer processes, respectively [42,43]. The average lifetime (τ_{ave} , Equation S7) was steadily decreased from BCN to CCNR-NPC/Pt (Table S5), due to the synergetic effects of enhancing internal-/interfacial vdW interactions in promoting exciton dissociation and directional photoelectron transfer from CCNR toward NPC and Pt acceptors [44]. Notably, as shown in Table S5, the relative percentage of τ_1 was increased from BCN (59.89%) to CCNR (69.15%), which is due to the higher crystallinity of CCNR, accounting for lower possibility of nonradiative charge recombination involving defect trapping (20.35%), relative to that of BCN (29.62%). In contrast, after forming CCNR/NPC interfacial vdW heterostructures, the relative percentage of τ_1 was otherwise progressively decreased for CCNR-NPC (58.76%) and CCNR-NPC/Pt (40.15%), which is owing to promoted interfacial transfer of both the free charge carriers and the undissociated excitons (that is, energy transfer) [45,46]. In Fig. 4d, the EPR peak at $g = 2.001$ reflects the unpaired electrons in the sp^2 -hybridized π -conjugated aromatic system [47]. After forming CCNR/NPC interfacial vdW heterostructures, EPR peak intensities are significantly enhanced in CCNR-NPC and CCNR-NPC/Pt, owing to facilitated π electrons redistribution and higher density of unpaired electrons [48].

The boosted charge utilization was further reflected by the photoelectrochemical measurements (Fig. 4e). The transient photocurrent densities were steadily increased from 0.11(BCN) to 1.19 $\mu A\ cm^{-2}$ (CCNR-NPC/Pt), as a result of inhibited radiative recombination, strengthened interfacial charge/exciton transfer and catalyzed charge utilization. Notably, a significant tailing is recorded for the photocurrent decay curves of CCNR-NPC and CCNR-NPC/Pt, due to the strong charge collection and storage capacity of NPC. Moreover, the wavelength-dependent photocurrent response (Fig. 4f) is monitored for CCNR-NPC/Pt, demonstrating the positive correlation between photocurrent density and the light absorption capacity, highlighting the great potential of CCNR-NPC/Pt for efficient conversion of solar energy into chemical energy via catalyzed photochemical reactions under full spectrum.

3.3. CO₂ adsorption behaviors

Higher specific surface area (S_{BET}) and porosity are beneficial for increasing CO₂ adsorption capacity [19]. Based on the N₂ sorption analyses (Fig. S5a, Table S2), the S_{BET} of CCNR (90.6 $m^2\ g^{-1}$) was almost increased exponentially, relative to that of BCN (9.6 $m^2\ g^{-1}$). High S_{BET} and porosity were largely inherited in CCNR-NPC and CCNR-NPC/Pt. Accordingly, the CO₂ adsorption capacities for CCNR-based photocatalysts are much higher than that of BCN (Fig. 5a). Interestingly, CCNR-NPC with somewhat lower S_{BET} (67.6 $m^2\ g^{-1}$) exhibited much higher CO₂ adsorption capability (0.480 mmol/g) than CCNR (0.348 mmol/g), suggesting the additional chemical adsorption of CO₂ [49]. This assumption is readily confirmed by the relatively faster nonlinear increase in CO₂ uptake in the P/P_0 range of 0–0.1, especially for CCNR-NPC/Pt with a maximal CO₂ uptake of 0.762 mmol/g.

To further disclose CO₂ adsorption behaviors, CO₂-TPD studies and density functional theory (DFT) calculations were performed. BCN exhibited only a minor CO₂-desorption peak at about 78 °C (Fig. 5b), corresponding to weak CO₂ adsorption on the basal planes of BCN (Figs. S8a and S9b) [31,50]. The calculated adsorption energy (E_{ads}) of CO₂ on the BCN surface is $-0.21\ eV$. In comparison, a significant increase in CO₂ adsorption capacity and intensity occurred for CCNR-based catalysts. Concretely, while a weak peak around 78 °C was retained, two additional stronger broad peaks emerged at around 160–170 °C and 409–491 °C, indicating new active sites in CCNR for CO₂-chemisorption. As demonstrated earlier, for CCNR, abundant K^+ are intercalated between CN layers, and abundant terminal NH_x are exposed at the CCNR edges, which would give rise to two additional kinds of active sites on the CCNR edge for adsorbing CO₂ molecules. First, the intercalated K^+ have strong interaction with the cave N atoms from adjacent upper and lower two CN layers, increasing electron densities on N atoms (Fig. 1i and Table S3), thus activating the exposed two-coordinated N from the triangular cave as grippers for capturing and bending CO₂ molecules (Fig. S9c) [25]. Second, the exposed terminal NH_x on the CCNR edge are active sites for adsorbing CO₂

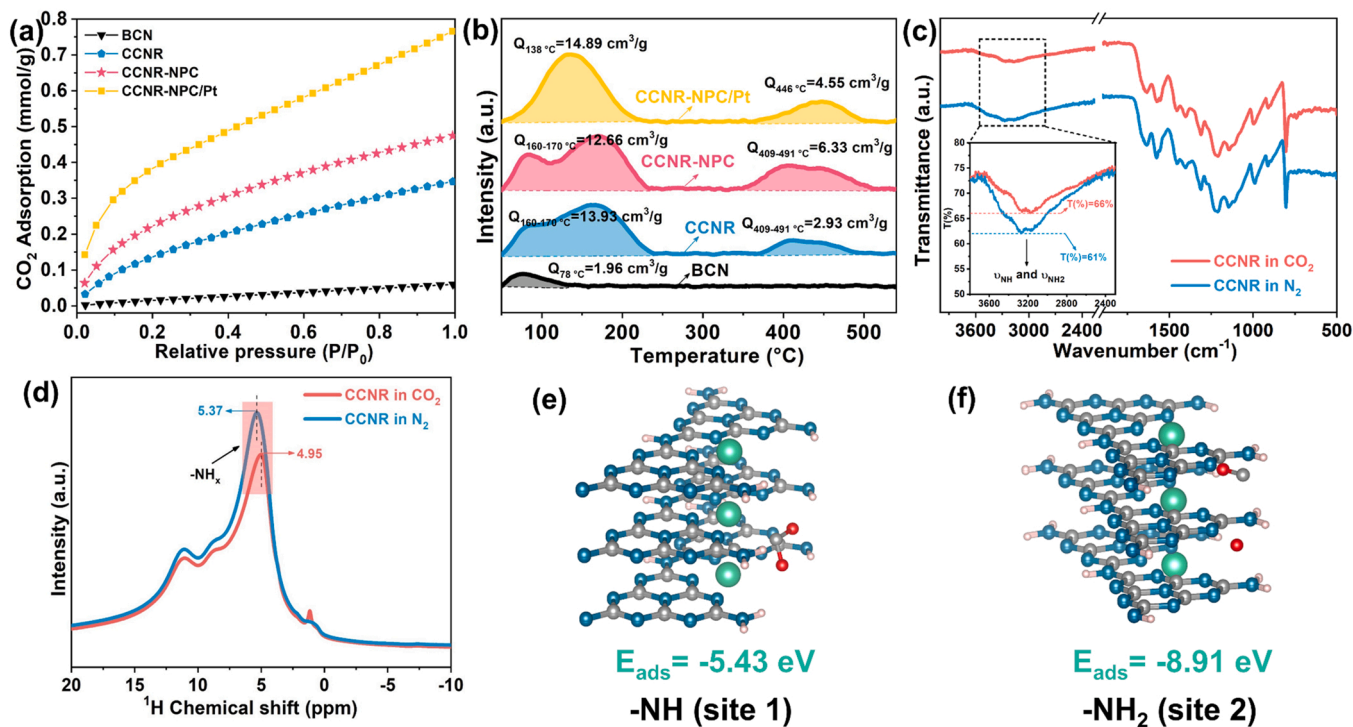


Fig. 5. CO₂ adsorption. (a) CO₂ adsorption curves and (b) CO₂-TPD profiles of typical samples; (c) FTIR spectra and (d) ¹H solid-state NMR spectra of N₂-purged and CO₂-purged CCNR; The CO₂ adsorption at two NH_x -sites on the CCNR edges: (e) CO₂ adsorption features at -NH (site 1) and (f) CO₂ adsorption features at -NH₂ (site 2), gray, blue, green, red and pink spheres represent C, N, K, O and H atoms, respectively.

molecules (Figs. S10 and S11). Notably, as a result of morphological variation, the dominant active sites for adsorbing CO_2 molecules changes from the basal planes of BCN to the edges of CCNR. The optimized configurations of adsorbed CO_2 at terminal NH_x on the CCNR edge are shown in Fig. 5e and f. Surprisingly, the calculated E_{ads} for CO_2 adsorbed on exposed terminal -NH site on CCNR edges (site 1, Fig. 5e) is -5.43 eV. The adsorbed CO_2 are activated with O-C-O bond angle of 108.9° , by forming hydrogen bonds between O atoms with terminal -NH of adjacent two layers. The CO_2 adsorbing on terminal -NH_2 of CCNR edges (site 2, Fig. 5f) is even stronger. After structural relaxation, an adsorbed CO_2 is dissociated into one adsorbed CO moiety and one adsorbed O atom. The O atom of adsorbed CO moiety also form hydrogen bonds with -NH_2 sites on the CCNR edge. For confirmation, FTIR and ^1H NMR spectra of N_2 -purged and CO_2 -purged CCNR were studied and compared. Obviously, the NH_x -related IR band was weakened by 5% after CO_2 exposure for CCNR (Fig. 5c), but not for BCN (Fig. S8b), demonstrating that exposed terminal NH_x groups on the CCNR edges were active for capturing CO_2 molecules. This was further confirmed by ^1H NMR spectra, in which the -NH_x associated NMR chemical shift signal (5.37 ppm) [51,52] was notably weakened in CO_2 -purged CCNR relative to that in N_2 -purged one (Fig. 5d). The active sites of CCNR for CO_2 adsorption were mostly retained in CCNR-NPC and CCNR-NPC/Pt, leaving comparable CO_2 -TPD profiles. The strengthened CO_2 adsorption on the CCNR edge will accelerate the photocatalytic CO_2RR by efficiently utilizing the radial photoelectrons.

3.4. Photocatalytic CO_2RR performance and mechanism

The photocatalytic CO_2RR performances were evaluated in the anaerobic environment without sacrificial agents. The raw GC signal identified CH_4 and CO as the main CO_2RR products, while the O_2 evolution is also detected as the oxidation product of H_2O (inset of Fig. S14). To confirm the carbon source of the detected products, ^{13}C -labeled CO_2RR over CCNR-NPC/Pt was monitored (Fig. 6c and S15). The recorded signal at $m/z = 17$ and $m/z = 29$ can be assigned to $^{13}\text{CH}_4$ and

^{13}CO , respectively, produced from $^{13}\text{CO}_2$, proving that CO_2 was at least one of the dominant carbon sources of CH_4 and CO. Moreover, control experiments were operated by replacing CO_2 with N_2 (Figs. S16a and b), and almost no carbon derivatives can be detected, further confirming that CH_4 and CO indeed originated from photocatalytic CO_2RR .

As expected, CCNR presented significantly improved CO_2RR efficiency compared with BCN (Fig. 6a), unfortunately, the main CO_2RR products were still limited to CO. By constructing CCNR-NPC vdW heterostructures, CO_2RR efficiency can further greatly increase. The optimized CCNR-NPC demonstrated CO and CH_4 average production rates of $1.358 \mu\text{mol h}^{-1} \text{g}^{-1}$ and $3.239 \mu\text{mol h}^{-1} \text{g}^{-1}$, respectively. More significantly, CO_2RR selectivity can be modulated over CCNR-NPC with directed photoelectron flows. It is probable that the escaped CO from CCNR can be further hydrogenated by utilizing axial photoelectrons on NPC, and thus more CH_4 can be produced with an optimal electron selectivity of 90.5%. In addition, relative to CCNR, HER was inhibited over CCNR-NPC, owing to the unique hydrophobicity (Fig. S12), and no H_2 was detected. A synergetic tuning of the internal/interfacial vdW interactions is essential for improving CO_2RR efficiency and selectivity over CCNR-NPC, which can be achieved by adjusting synthesis procedures including the ratio of raw materials and the thermal polymerization route (Fig. S16a). Moreover, the CO_2RR performance can be further boosted by decorating Pt moieties on NPC as cocatalysts stabilizing CO intermediate and catalyzing CO hydrogenation. Remarkably, the 2 wt% Pt-decorated CCNR-NPC presented outstanding CH_4 selectivity of 90.2%, and the average CH_4 yield rate was reaching $11.793 \mu\text{mol h}^{-1} \text{g}^{-1}$ (Fig. 6b), which is among the best of reported $\text{g-C}_3\text{N}_4$ -based photocatalysts for efficient and selective CO_2RR (Table S6). The host-guest interactions, chemical states and loading amount of Pt species are important factors affecting the CO_2RR efficiency and selectivity over Pt-decorated series photocatalysts (Fig. 6b and S16b).

The wavelength-dependent photocatalytic CO_2RR activities were also investigated over CCNR-NPC/Pt, which were in good agreement with optical absorption capacity (Fig. S16d), demonstrating the efficient conversion and utilization of solar energy, and the apparent quantum

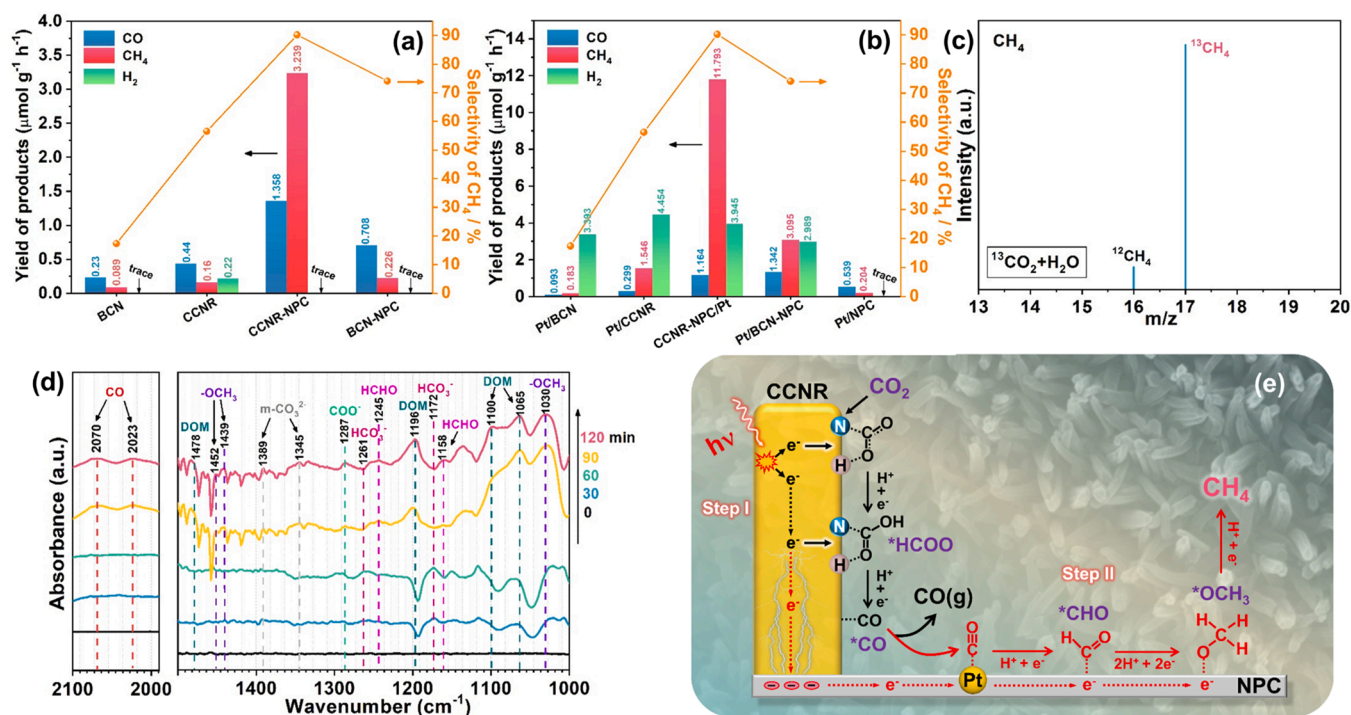


Fig. 6. (a) Photocatalytic CO_2RR performance of BCN, CCNR, CCNR-NPC and BCN-NPC under full-spectrum light irradiation. (b) Photocatalytic CO_2RR performance of Pt-decorated samples. (c) The ^{13}C -labeling GC-MS signal after background corrections. (d) *In situ* DRIFTS spectra for Photocatalytic CO_2RR on CCNR-NPC/Pt in the wavenumber ranges of 1000–1500 cm^{-1} and 2000–2100 cm^{-1} . (e) The possible tandem photocatalytic CO_2RR processes over CCNR-NPC/Pt.

yield (AQY) at the wavelength of 420 nm is reaching 0.41% (Table S4). The wide spectrum CO₂RR activity of CCNR-NPC/Pt is also demonstrated under AM 1.5 G irradiation (Fig. S16b). Moreover, the considerable stability and recyclability of CCNR-NPC/Pt were well demonstrated by a five-run cycling activity test (Fig. S16c). Meanwhile, XRD, FTIR and XPS spectra (Fig. S17) of CCNR-NPC/Pt before and after CO₂RR service kept almost unchanged, confirming the structural stability.

The photocatalytic CO₂RR process over CCNR-NPC/Pt photocatalysts was further explored by in situ DRIFT spectra (Fig. 6d and S18a). Before light irradiation, two CO₂ adsorption configuration ($m\text{-CO}_3^{2-}$ at 1345 and 1389 cm⁻¹; HCO_3^- at 1172 and 1261 cm⁻¹) are recorded. The HCO_3^- might be derived from CO₂ adsorbed at terminal NH_x -sites on the CCNR edge [53]. After light illumination, the HCO_3^- quickly disappeared and a new COO^- peak at 1287 cm⁻¹ emerged [19, 54,55]. The COO^- is originated from surface-activated CO₂ involving one-electron transfer. Meanwhile, multiple reduction intermediates were detected and progressively enhanced in intensity with prolonging irradiation time, including formate species (HCOO^- at 1725, 1737, 1767 and 1787 cm⁻¹), formaldehyde (HCHO at 1158, 1245 and 1710 cm⁻¹), methoxyl groups ($-\text{OCH}_3$ at 1030, 1439 and 1452 cm⁻¹) and dioxy-methylene (DOM at 1065, 1100, 1196 and 1478 cm⁻¹) [49,56]. Significantly, the surface-bound CO intermediate (1800–2100 cm⁻¹) was gradually accumulated on CCNR-NPC/Pt, but not on CCNR (Fig. S18b). According to Fig. S18c, the weak CO adsorption energy ($E_{\text{ads}} = -0.19$ eV) reveal that $^*\text{CO}$ vastly prefers to desorb from the CCNR edge for CO generation [19]. In contrast, stronger CO affinity to NPC and the immobilized Pt active sites can be clearly reflected by CO-DRIFTS results (Fig. 3f and S19). The stabilized CO intermediates are conducive to accelerating further hydrogenation and generating CH₄ [22].

Based on the in situ DRIFTS results, the possible reaction pathways of tandem CO₂ photoconversion over CCNR-NPC/Pt were proposed as illustrated in Fig. 6e. Two major steps were involved: (I) Initially, the CCNR edge-adsorbed CO₂ (HCO_3^- and COO^-) on NH_x sites were reduced into $^*\text{HCOO}$ via proton coupled electron transfer, which was then dehydrated into $^*\text{CO}$. CO will escape from the CCNR edge due to low affinity ($E_{\text{ads}} = -0.19$ eV). (II) Due to stronger CO affinity, the NPC/Pt active sites would actively capture escaped CO intermediate. Meanwhile, taking advantage of the multifunctional electron trapping ability and co-catalytic effects, the captured $^*\text{CO}$ will go through further hydrogenation to evolve $^*\text{CHO}$ and $^*\text{OCH}_3$, and finally, generate CH₄ products. In this connection, a tandem CO₂ photoconversion system is established for highly selective CH₄ generation over CCNR-NPC/Pt.

4. Conclusion

In summary, we demonstrated that the synergy of internal and interfacial vdW heterostructures within g-C₃N₄ can be well integrated to synergistically enhance the radial and axial charge dynamics. Meanwhile, NH_x sites on the CCNR edge and NPC immobilized Pt active sites serve as the tandem catalytic active platforms for highly efficient CO₂ conversion and selective CH₄ production. Especially, an increase of 132.5 times in the CH₄ yield was achieved over CCNR-NPC/Pt, reaching 11.79 $\mu\text{mol g}^{-1} \text{h}^{-1}$ with a selectivity of 90.2%, relative to pristine BCN. This work not only offers a new strategy for constructing g-C₃N₄-based vdW heterostructure toward efficient and selective photocatalytic CO₂RR by maneuvering charge transfer direction and dynamics, but also provides insights into tandem CO₂ photoconversion over spatially separated but cooperative two reduction active centers.

CRediT authorship contribution statement

Xi Wu: Investigation, Writing – original draft. **Ruiyu Zhong:** Investigation. **Xudong Lv:** Investigation. **Zhuofeng Hu:** Theoretical calculation. **Dehua Xia:** Writing – review & editing. **Chuanhao Li:** Writing – review & editing. **Bo Song:** Writing – review & editing.

Shengwei Liu: Conceptualization, Supervision, Writing – review & editing, Funding acquisition.

Declaration of competing interest

The authors declare that they have no known competing financial interests or personal relationships that could have appeared to influence the work reported in this paper.

Data Availability

Data will be made available on request.

Acknowledgements

This work was financially supported by the National Natural Science Foundation of China (51872341), the Tip-top Scientific and Technical Innovative Youth Talents of Guangdong Special Support Program (2019TQ05L196) and the Science and Technology Planning Project of Guangdong Province (2021A1515010147). The theoretical calculation is supported by National supercomputer center in Guangzhou and National supercomputing center in Shenzhen (Shenzhen cloud computing center).

Appendix A. Supporting information

Supplementary data associated with this article can be found in the online version at doi:10.1016/j.apcatb.2023.122666.

References

- [1] M. Halmann, Photoelectrochemical reduction of aqueous carbon dioxide on p-type gallium phosphide in liquid junction solar cells, *Nature* 275 (1978) 115–116, <https://doi.org/10.1038/275115a0>.
- [2] J. Ran, M. Jaroniec, S.Z. Qiao, Cocatalysts in semiconductor-based photocatalytic CO₂ reduction: achievements, challenges, and opportunities, *Adv. Mater.* 30 (2018), 1704649, <https://doi.org/10.1002/adma.201704649>.
- [3] M. Sayed, F. Xu, P. Kuang, J. Low, S. Wang, L. Zhang, J. Yu, Sustained CO₂-photoreduction activity and high selectivity over Mn, C-codoped ZnO core-triple shell hollow spheres, *Nat. Commun.* 12 (2021) 4936, <https://doi.org/10.1038/s41467-021-25007-6>.
- [4] S. Wageh, A. Al-Ghamdi, L. Liu, S-scheme heterojunction photocatalyst for CO₂ photoreduction, *Acts Phys. -Chim. Sin.* 37 (2021), 2010024, <https://doi.org/10.3866/pku.whxb202010024>.
- [5] L. Wang, B. Zhu, J. Zhang, J. Ghasemi, M. Mousavi, J. Yu, S-scheme heterojunction photocatalysts for CO₂ reduction, *Matter* 5 (2022) 4187–4211, <https://doi.org/10.1016/j.matt.2022.09.009>.
- [6] G. Zhang, G. Li, T. Heil, S. Zafeiratos, F. Lai, A. Savateev, M. Antonietti, X. Wang, Tailoring the grain boundary chemistry of polymeric carbon nitride for enhanced solar hydrogen production and CO₂ reduction, *Angew. Chem. Int. Ed.* 58 (2019) 3433–3437, <https://doi.org/10.1002/anie.201811938>.
- [7] X. Fei, H. Tan, B. Cheng, B. Zhu, L. Zhang, 2D/2D black phosphorus/g-C₃N₄ S-scheme heterojunction photocatalysts for CO₂ reduction investigated using DFT calculations, *Acta Phys. -Chim. Sin.* 37 (2021), 2010027, <https://doi.org/10.3866/pku.whxb202010027>.
- [8] Y. Kang, Y. Yang, L.C. Yin, X. Kang, L. Wang, G. Liu, H.M. Cheng, Selective breaking of hydrogen bonds of layered carbon nitride for visible light photocatalysis, *Adv. Mater.* 28 (2016) 6471–6477, <https://doi.org/10.1002/adma.201601567>.
- [9] L. Lin, Z. Lin, J. Zhang, X. Cai, W. Lin, Z. Yu, X. Wang, Molecular-level insights on the reactive facet of carbon nitride single crystals photocatalysing overall water splitting, *Nat. Catal.* 3 (2020) 649–655, <https://doi.org/10.1038/s41929-020-0476-3>.
- [10] Y. Xia, Z. Tian, T. Heil, A. Meng, B. Cheng, S. Cao, J. Yu, M. Antonietti, Highly selective CO₂ capture and its direct photochemical conversion on ordered 2D/1D heterojunctions, *Joule* 3 (2019) 2792–2805, <https://doi.org/10.1016/j.joule.2019.08.011>.
- [11] G. Zhang, J. Zhu, Y. Xu, C. Yang, C. He, P. Zhang, Y. Li, X. Ren, H. Mi, In-plane charge transport dominates the overall charge separation and photocatalytic activity in crystalline carbon nitride, *ACS Catal.* 12 (2022) 4648–4658, <https://doi.org/10.1021/acscatal.2c00233>.
- [12] G. Zhang, Y. Xu, D. Yan, C. He, Y. Li, X. Ren, P. Zhang, H. Mi, Construction of K⁺ ion gradient in crystalline carbon nitride to accelerate exciton dissociation and charge separation for visible light H₂ production, *ACS Catal.* 11 (2021) 6995–7005, <https://doi.org/10.1021/acscatal.1c00739>.
- [13] J. Li, Z. Zhang, W. Cui, H. Wang, W. Cen, G. Johnson, G. Jiang, S. Zhang, F. Dong, The spatially oriented charge flow and photocatalysis mechanism on internal van

- der Waals heterostructures enhanced g-C₃N₄, *ACS Catal.* 8 (2018) 8376–8385, <https://doi.org/10.1021/acscatal.8b02459>.
- [14] K. Novoselov, A. Mishchenko, A. Carvalho, A. Castro Neto, 2D materials and van der Waals heterostructures, *Science* 353 (2016) 6298, <https://doi.org/10.1126/science.aac9436>.
- [15] J. Jiang, D. Duan, J. Ma, Y. Jiang, R. Long, C. Gao, Y. Xiong, Van der Waals heterostructures by single cobalt sites-anchored graphene and g-C₃N₄ nanosheets for photocatalytic syngas production with tunable CO/H₂ ratio, *Appl. Catal. B* 295 (2021), 120261, <https://doi.org/10.1016/j.apcatb.2021.120261>.
- [16] J. Ran, W. Guo, H. Wang, B. Zhu, J. Yu, S.-Z. Qiao, Metal-free 2D/2D phosphorene/g-C₃N₄ van der Waals heterojunction for highly enhanced visible-light photocatalytic H₂ production, *Adv. Mater.* 30 (2018), 1800128, <https://doi.org/10.1002/adma.201800128>.
- [17] I. Gerber, P. Serp, A theory/experience description of support effects in carbon-supported catalysts, *Chem. Rev.* 120 (2019) 1250–1349, <https://doi.org/10.1021/acs.chemrev.9b00209>.
- [18] Z. Zhang, Y. Chen, L. Zhou, C. Chen, Z. Han, B. Zhang, Q. Wu, L. Yang, L. Du, Y. Bu, P. Wang, X. Wang, H. Yang, Z. Hu, The simplest construction of single-site catalysts by the synergism of micropore trapping and nitrogen anchoring, *Nat. Commun.* 10 (2019) 1657, <https://doi.org/10.1038/s41467-019-09596-x>.
- [19] X. Li, W. He, C. Li, B. Song, S. Liu, Synergetic surface modulation of ZnO/Pt@ZIF-8 hybrid nanorods for enhanced photocatalytic CO₂ valorization, *Appl. Catal. B* 287 (2021) 119934, <https://doi.org/10.1016/j.apcatb.2021.119934>.
- [20] J. Gao, H. Zhang, X. Guo, J. Luo, S.M. Zakeeruddin, D. Ren, M. Grätzel, Selective C–C coupling in carbon dioxide electroreduction via efficient spillover of intermediates as supported by operando raman spectroscopy, *J. Am. Chem. Soc.* 141 (2019) 18704–18714, <https://doi.org/10.1021/jacs.9b07415>.
- [21] H. Zhang, X. Chang, J.G. Chen, W.A. Goddard, B. Xu, M.-J. Cheng, Q. Lu, Computational and experimental demonstrations of one-pot tandem catalysis for electrochemical carbon dioxide reduction to methane, *Nat. Commun.* 10 (2019) 3340, <https://doi.org/10.1038/s41467-019-11292-9>.
- [22] W. Wang, C. Deng, S. Xie, Y. Li, W. Zhang, H. Sheng, C. Chen, J. Zhao, Photocatalytic C–C coupling from carbon dioxide reduction on copper oxide with mixed-valence copper(I)/copper(II), *J. Am. Chem. Soc.* 143 (2021) 2984–2993, <https://doi.org/10.1021/jacs.1c02066>.
- [23] P. Liu, Z. Huang, X. Gao, X. Hong, J. Zhu, G. Wang, Y. Wu, J. Zeng, X. Zheng, Synergy between palladium single atoms and nanoparticles via hydrogen spillover for enhancing CO₂ photoreduction to CH₄, *Adv. Mater.* 34 (2022), 2200057, <https://doi.org/10.1002/adma.202200057>.
- [24] S.-F. Ng, J.-J. Foo, W.-J. Ong, Solar-powered chemistry: engineering low-dimensional carbon nitride-based nanostructures for selective CO₂ conversion to C₁–C₂ products, *InfoMat* 4 (2022), e12279, <https://doi.org/10.1002/inf2.12279>.
- [25] Y. Liang, X. Wu, X. Liu, C. Li, S. Liu, Recovering solar fuels from photocatalytic CO₂ reduction over W⁶⁺-incorporated crystalline g-C₃N₄ nanorods by synergetic modulation of active centers, *Appl. Catal. B* 304 (2022), 120978, <https://doi.org/10.1016/j.apcatb.2021.120978>.
- [26] D.-L. Meng, M.-D. Zhang, D.-H. Si, M.-J. Mao, Y. Hou, Y.-B. Huang, R. Cao, Highly selective tandem electroreduction of CO₂ to ethylene over atomically isolated nickel-nitrogen site/copper nanoparticle, *Angew. Chem. Int. Ed.* 60 (2021) 25485, <https://doi.org/10.1002/anie.202111136>.
- [27] C. Chen, Y. Li, S. Yu, S. Louisiana, J. Jin, M. Li, M.B. Ross, P. Yang, Cu–Ag tandem catalysts for high-rate CO₂ electrolysis toward multicarbons, *Joule* 4 (2020) 1688–1699, <https://doi.org/10.1016/j.joule.2020.07.009>.
- [28] W. Ren, J. Cheng, H. Ou, C. Huang, M. Anpo, X. Wang, Optimizing the crystallization process of conjugated polymer photocatalysts to promote electron transfer and molecular oxygen activation, *J. Catal.* 389 (2020) 636–645, <https://doi.org/10.1016/j.jcat.2020.07.005>.
- [29] S. Liu, F. Chen, S. Li, X. Peng, Y. Xiong, Enhanced photocatalytic conversion of greenhouse gas CO₂ into solar fuels over g-C₃N₄ nanotubes with decorated transparent ZIF-8 nanoclusters, *Appl. Catal. B* 211 (2017) 1–10, <https://doi.org/10.1016/j.apcatb.2017.04.009>.
- [30] X. Wu, C. Lu, J. Liu, S. Song, C. Sun, Constructing efficient solar light photocatalytic system with Ag-introduced carbon nitride for organic pollutant elimination, *Appl. Catal. B* 217 (2017) 232–240, <https://doi.org/10.1016/j.apcatb.2017.06.001>.
- [31] P. Xia, B. Zhu, J. Yu, S. Cao, M. Jaroniec, Ultra-thin nanosheet assemblies of graphitic carbon nitride for enhanced photocatalytic CO₂ reduction, *J. Mater. Chem. A* 5 (2017) 3230–3238, <https://doi.org/10.1039/c6ta08310b>.
- [32] M. Yang, R. Lian, X. Zhang, C. Wang, J. Cheng, X. Wang, Photocatalytic cyclization of nitrogen-centered radicals with carbon nitride through promoting substrate/catalyst interaction, *Nat. Commun.* 13 (2022) 4900, <https://doi.org/10.1038/s41467-022-32623-3>.
- [33] Y. Xie, Y. Zhuo, S. Liu, Y. Lin, D. Zuo, X. Wu, C. Li, P.K. Wong, Ternary g-C₃N₄/ZnNCN@ZIF-8 hybrid photocatalysts with robust interfacial interactions and enhanced CO₂ reduction performance, *Sol. RRL* 4 (2020), 1900440, <https://doi.org/10.1002/solr.201900440>.
- [34] H. Xiao, W.A. Goddard III, T. Cheng, Y. Liu, Cu metal embedded in oxidized matrix catalyst to promote CO₂ activation and CO dimerization for electrochemical reduction of CO₂, *Proc. Natl. Acad. Sci.* 114 (2017) 6685–6688, <https://doi.org/10.1073/pnas.1702405114>.
- [35] S. Chen, J. Bi, Y. Zhao, L. Yang, C. Zhang, Y. Ma, Q. Wu, X. Wang, Z. Hu, Nitrogen-doped carbon nanocages as efficient metal-free electrocatalysts for oxygen reduction reaction, *Adv. Mater.* 24 (2012) 5593–5597, <https://doi.org/10.1002/adma.201202424>.
- [36] H. Zhang, Q. Liu, Y. Fang, C. Teng, X. Liu, P. Fang, Y. Tong, X. Lu, Boosting Zn-ion energy storage capability of hierarchically porous carbon by promoting chemical adsorption, *Adv. Mater.* 31 (2019), 1904948, <https://doi.org/10.1002/adma.201904948>.
- [37] T. Xiong, W. Cen, Y. Zhang, F. Dong, Bridging the g-C₃N₄ interlayers for enhanced photocatalysis, *ACS Catal.* 6 (2016) 2462–2472, <https://doi.org/10.1021/acscatal.5b02922>.
- [38] A. Li, Q. Cao, G. Zhou, B.V. Schmidt, W. Zhu, X. Yuan, H. Huo, J. Gong, M. Antonietti, Three-phase photocatalysis for the enhanced selectivity and activity of CO₂ reduction on a hydrophobic surface, *Angew. Chem. Int. Ed.* 131 (2019) 14691–14697, <https://doi.org/10.1002/anie.201908058>.
- [39] L. Zhang, R. Long, Y. Zhang, D. Duan, Y. Xiong, Y. Zhang, Y. Bi, Direct observation of dynamic bond evolution in single-atom Pt/C₃N₄ catalysts, *Angew. Chem. Int. Ed.* 59 (2020) 6224–6229, <https://doi.org/10.1002/anie.201915774>.
- [40] B. Han, Y. Guo, Y. Huang, W. Xi, J. Xu, J. Luo, H. Qi, Y. Ren, X. Liu, B. Qiao, Strong metal–support interactions between Pt single atoms and TiO₂, *Angew. Chem. Int. Ed.* 59 (2020) 11824–11829, <https://doi.org/10.1002/anie.202003208>.
- [41] C. Lv, Y. Qian, C. Yan, Y. Ding, Y. Liu, G. Chen, G. Yu, Defect engineering metal-free polymeric carbon nitride electrocatalyst for effective nitrogen fixation under ambient conditions, *Angew. Chem. Int. Ed.* 130 (2018) 10403–10407, <https://doi.org/10.1002/anie.201806386>.
- [42] F. Xu, K. Meng, B. Cheng, S. Wang, J. Xu, J. Yu, Unique S-scheme heterojunctions in self-assembled TiO₂/CsPbBr₃ hybrids for CO₂ photoreduction, *Nat. Commun.* 11 (2020) 4613, <https://doi.org/10.1038/s41467-020-18350-7>.
- [43] M. Liu, S. Wageh, A.A. Al-Ghamdi, P. Xia, B. Cheng, L. Zhang, J. Yu, Quenching induced hierarchical 3D porous g-C₃N₄ with enhanced photocatalytic CO₂ reduction activity, *Chem. Commun.* 55 (2019) 14023–14026, <https://doi.org/10.1039/c9cc07647f>.
- [44] Z. Hu, X. Liu, P.L. Hernández-Martínez, S. Zhang, P. Gu, W. Du, W. Xu, H.V. Demir, H. Liu, Q. Xiong, Interfacial charge and energy transfer in van der Waals heterojunctions, *InfoMat* 4 (2022), e12290, <https://doi.org/10.1002/inf2.12290>.
- [45] M. Shalom, S. Inal, C. Fettkenhauer, D. Neher, M. Antonietti, Improving carbon nitride photocatalysis by supramolecular preorganization of monomers, *J. Am. Chem. Soc.* 135 (2013) 7118–7121, <https://doi.org/10.1021/ja402521s>.
- [46] P. Kumar, E. Vahidzadeh, U.K. Thakur, P. Kar, K.M. Alam, A. Goswami, N. Mahdi, K. Cui, G.M. Bernard, V.K. Michaelis, C₃N₄: A low bandgap semiconductor containing an azo-linked carbon nitride framework for photocatalytic, photovoltaic and adsorbent applications, *J. Am. Chem. Soc.* 141 (2019) 5415–5436, <https://doi.org/10.1021/jacs.9b00144>.
- [47] J. Zhang, M. Zhang, C. Yang, X. Wang, Nanospherical carbon nitride frameworks with sharp edges accelerating charge collection and separation at a soft photocatalytic interface, *Adv. Mater.* 26 (2014) 4121–4126, <https://doi.org/10.1002/adma.201400573>.
- [48] P. Xia, M. Liu, B. Cheng, J. Yu, L. Zhang, Dopamine modified g-C₃N₄ and its enhanced visible-light photocatalytic H₂-production activity, *ACS Sustain. Chem. Eng.* 6 (2018) 8945–8953, <https://doi.org/10.1021/acssuschemeng.8b01300>.
- [49] X. Liu, M. Ye, S. Zhang, G. Huang, C. Li, J. Yu, P.K. Wong, S. Liu, Enhanced photocatalytic CO₂ valorization over TiO₂ hollow microspheres by synergetic surface tailoring and Au decoration, *J. Mater. Chem. A* 6 (2018) 24245–24255, <https://doi.org/10.1039/c8ta09661a>.
- [50] H.-Z. Wu, S. Bandaru, J. Liu, L.-L. Li, Z. Wang, Adsorption of H₂O, H₂, O₂, CO, NO, and CO₂ on graphene/g-C₃N₄ nanocomposite investigated by density functional theory, *Appl. Surf. Sci.* 430 (2018) 125–136, <https://doi.org/10.1016/j.apsusc.2017.06.073>.
- [51] X. Bao, M. Liu, Z. Wang, D. Dai, P. Wang, H. Cheng, Y. Liu, Z. Zheng, Y. Dai, B. Huang, Photocatalytic selective oxidation of HMF coupled with H₂ evolution on flexible ultrathin g-C₃N₄ nanosheets with enhanced N–H interaction, *ACS Catal.* 12 (2022) 1919–1929, <https://doi.org/10.1021/acscatal.1c05357>.
- [52] S. Rawool, A. Samanta, T. Ajithkumar, Y. Kar, V. Polshettiwar, Photocatalytic hydrogen generation and CO₂ conversion using g-C₃N₄ decorated dendritic fibrous nanosilica: Role of interfaces between silica and g-C₃N₄, *ACS Appl. Energy Mater.* 3 (2020) 8150–8158, <https://doi.org/10.1021/acsaem.0c01265>.
- [53] W. Su, J. Zhang, Z. Feng, T. Chen, P. Ying, C. Li, Surface phases of TiO₂ nanoparticles studied by UV Raman spectroscopy and FT-IR spectroscopy, *J. Phys. Chem. C* 112 (2008) 7710–7716, <https://doi.org/10.1021/jp7118422>.
- [54] M. Yamamoto, T. Yoshida, N. Yamamoto, T. Nomoto, Y. Yamamoto, S. Yagi, H. Yoshida, Photocatalytic reduction of CO₂ with water promoted by Ag clusters in Ag/Ga₂O₃ photocatalysts, *J. Mater. Chem. A* 3 (2015) 16810–16816, <https://doi.org/10.1039/c5ta04815j>.
- [55] L. Liu, Y. Jiang, H. Zhao, J. Chen, J. Cheng, K. Yang, Y. Li, Engineering coexposed {001} and {101} facets in oxygen-deficient TiO₂ nanocrystals for enhanced CO₂ photoreduction under visible light, *ACS Catal.* 6 (2016) 1097–1108, <https://doi.org/10.1021/acscatal.5b02098>.
- [56] W.-C. Wu, C.-C. Chuang, J.-L. Lin, Bonding geometry and reactivity of methoxy and ethoxy groups adsorbed on powdered TiO₂, *J. Phys. Chem. B* 104 (2000) 8719–8724, <https://doi.org/10.1021/jp0017184>.